Exploring wind-driven subsurface water flow with an acoustic Doppler velocity profiler

Rémi Chemin, Guillemette Caulliez

Exploring wind-driven subsurface water flow with an acoustic Doppler velocity profiler

Rémi Chemin and Guillemette Caulliez*

Aix-Marseille Université, Université de Toulon, CNRS, IRD, Mediterranean Institute of Oceanography (MIO), UM 110, Marseille, France

Corresponding author address: Institut Méditerranéen d'Océanologie, 163, avenue de Luminy - bat. IOA, case 901, 13288 Marseille Cedex 09, France

E-mail: guillemette.caulliez@mio.osupytheas.fr

ABSTRACT

In this study, we report on experiments carried out in a large wind-wave tank to investigate the potential of the acoustic Doppler velocity profiler for determining the structure of the subsurface water boundary layer. This flow located just beneath the air-water interface forms whenever wind blows. The profiler is first tested for a steady flow generated by pumps beneath a flat water surface. Measurements of the velocity field at different stages of development of the wind-induced shear flow, from laminar to fully-turbulent, are then analyzed. The best way to obtain reliable data under these flow conditions is thoroughly examined. Despite the inherent difficulty of seeding acoustic tracers homogeneously in such a boundary layer, the profiler has the major advantage of providing records of the instantaneous profiles of the subsurface velocity field referenced to surface elevation. This feature makes it possible to estimate statistical properties of the water motions at various scales in a wave-following coordinate system, and thus greatly increases the physical significance of the measured quantities. The variation with fetch of the main characteristics of the mean drift current, orbital wave motions and turbulent flow disturbances estimated in this coordinate system is then presented and discussed in detail.

1. Introduction

Turbulent motions generated in the thin water boundary layer driven by wind and waves at the free surface play a key role in heat and mass exchanges across the air-sea interface. They control processes of critical importance for predicting air-sea interaction and behavior of many natural environment systems, such as the transfer of greenhouse gases and the dispersion of pollutants and micro-organisms. However, the experimental investigation of water surface flow dynamics remains very challenging because of the inherent difficulty of performing non-intrusive measurements just beneath a moving air-water interface of complex and highly variable geometry. Another difficulty lies in the structure of the subsurface water boundary layer in which several instability processes coexist and interplay, generating motions of comparable magnitude and which overlap in the space-time domain. Therefore, the properties of the mean shear current, orbital wave motions, and other organized and turbulent motions of various scales occurring in water are still poorly known.

Over the last decades, better knowledge of the small-scale processes within the surface sublayer has been achieved by using sophisticated optical techniques, such as infrared imaging, laser Doppler or particle image velocimetry. However, the new insights are confined to a limited number of specific experimental conditions for which one of the processes involved is essentially dominant such as wave microbreaking or initial generation of shear flow and turbulence (Thais and Magnaudet 1996; Banner and Peirson 1998; Peirson and Banner 2003; Siddiqui et al. 2001; Veron and Melville 2001; Caulliez et al. 2007). Furthermore, there is still a significant gap in our understanding between the detailed description of individual phenomena as provided by spatial imaging techniques and the statistical flow properties as estimated from time measurements by single-point instruments.

Meanwhile, a technique for measuring water velocity fields remotely by means of acoustic pulses has been developed. Based on the Doppler effect, it was designed and further improved primarily for conducting ocean observations. The spatial resolution and accuracy of these measurements have been gradually increased by the implementation of advanced techniques or new probing concepts, enabling the assessment of the water turbulence behavior. More recently, a further step forward has been achieved with the commercial launch of the acoustic Doppler velocity Vectrino profiler by Nortek. This instrument offers the means to measure the three water velocity components along a short flow segment with relatively high space and time resolution (1 mm and 0.01 s). This ready-to-use device thus enables the investigation of the small-scale dynamics of turbulent flows as currently observed within boundary layers over various types of bed-water interface in laboratory, lakes, rivers or coastal zones (Rusello and Allard 2012; Thomas and McLelland 2015; Brand et al. 2016; Koca et al. 2017; Leng and Chanson 2017). However, to our knowledge, no detailed study of the capabilities of this new probe for describing the complex structure of the natural free surface boundary layers has been undertaken yet. The aim of the present work is to address this question.

After a brief description of the instrument and the experimental procedure adopted in this study, we first examine the performance of the acoustic Doppler velocity profiler for measuring the velocity field just below the air-water interface when this instrument is deployed in a steady flow generated by water pumps. Then, the observations made by the Vectrino profiler within the wind-driven subsurface water boundary layer are presented in detail. They enable us to characterize with a good accuracy the variations of the mean and fluctuating flow features when the surface boundary layer changes spatially from a laminar to a fully-developed turbulent structure.

2. Experimental arrangement

a. Experimental configuration

The tests of the Vectrino profiler and the observations performed with this instrument for investigating the water surface flow were carried out in the large *UMS Pytheas* wind-wave facility in Marseille-Luminy (Fig.1a). The facility is composed of a 40 m long, 2.6 m wide, and 0.9 m deep water tank and an air channel 1.5 m in height at the test section. The air flow is generated by an axial fan located in the recirculation flume and then passes through divergent and convergent sections including a settling chamber equipped with turbulence grids. This arrangement facilitates the generation of a homogeneous and very low-turbulence wind at the entrance to the test section. The computer-controlled wind speed can vary between 1 and 15 m s^{-1}. In addition, two water pumps can generate a steady current of a few centimeters per second throughout the tank. At the end of the flume, a long permeable beach damps the wave reflection. In order to investigate the coupled generation of wind waves and surface drift current at short fetches without any influence of preexisting turbulence in the air, particular attention was focused on the air-water junction at the entrance to the water tank, to make it as smooth as possible. To this end, the junction between the bottom floor of the air channel and the water surface was leveled by a 1.5 m long weakly-inclined floating device fixed at the end of the air duct. This prevents the development of large-scale air flow disturbances within the water surface boundary layer for all wind speed conditions.

The water flow driven by wind inside the subsurface boundary layer was investigated by means of a Nortek Vectrino Acoustic Doppler Velocimeter Profiler (referenced as profiler or ADVP). Its mode of operation and its set up will be detailed in Sect.2b. The water surface flow velocity was monitored using Particle Tracking Velocimetry (PTV). For this purpose, small paper drifters were injected from the air flow just above the water surface two meters upstream of the measuring

section and their motions were recorded by a video camera looking down vertically from the top of the tunnel. The field of view was 0.2 m in the wind direction with the head of the profiler visible in the downwind part of the image to provide a precise fetch reference. On average, for one flow condition, twenty drifters were monitored by the camera at a frame rate of 5 Hz. The images were then processed by using the PTV algorithm developed by Brevis et al. (2011).

To observe wind wave growth simultaneously with drift current development, water surface displacements were measured by two high resolution capacitance wave gauges 8 mm apart streamwise and located 45 mm downstream of the center of the ADVP transceiver. To avoid ripple disturbances generated at the water surface by any rigid mount, these probes are made of two thin sensitive wires (0.3 mm in diameter) hung vertically in the water with a weight. The phase velocity of dominant waves is determined from both wave signals using a cross-spectral method. Both components of the water surface slope were also measured by a single-point laser slope gauge. As first described by Lange et al. (1982), this system is based on the detection of the refraction angle of a He-Ne laser beam at the water surface by an optical receiver. The latter includes a Fresnel lens, a diffusing screen and a dual-axis position sensing diode. The He-Ne laser was mounted vertically at the top of the tunnel and the receiver was immersed at a depth of 0.4 m below the water surface and centered at the same fetch 0.35 m spanwise from the profiler head. To make visualizations easier, all instruments were set up at the test section of the air tunnel equipped with large glass windows located 28 m from the entrance to the tank. To adjust the fetch X, the water surface was covered by a long floating plastic sheet of appropriate length. The fetch refers here to the distance between the downwind edge of the plastic sheet and the profiler head. The reference wind velocity was measured with a Pitot tube located at the center of the tunnel, 0.7 m above the water level at rest and 8 m upwind of the profiler.

b. The Acoustic Doppler Velocimeter Profiler

The Nortek Vectrino profiler is a multi-static acoustic Doppler velocimeter that can measure simultaneously the three water velocity components over a 30 mm long flow section with a spatial resolution as fine as 1 mm and a sampling rate of up to 100 Hz. The sensor head of the device consists of a central active transducer, 6 mm in diameter and emitting at a 10 MHz frequency, surrounded symmetrically by an array of four receivers positioned in two perpendicular vertical planes with a slanting angle of 30 deg towards the center (see Nortek (2013)). This probe was mounted on a fixed, 0.36 m long rigid stem connected to the main waterproof electronics housing. It was deployed vertically in the upward-looking position at a variable distance from the water surface but with the latter generally embedded within the measuring profile. The lowest sample cell of the profile is located 40 mm above the central emitter, i.e. in a region where the flow disturbances caused by the probe are mostly negligible (Rusello et al. 2006). The instrument used in these experiments was owned by Nortek-Med and was operating with the 2013 MIDAS Software to control and collect data.

This high-resolution profiler uses a pulse-to-pulse coherent Doppler procedure for measuring instantaneous scattering particle velocity at the intersection of the acoustic transmitter and receiver beams, as first described by Lhermitte and Serafin (1984). Its mode of operation as well as its measurement capabilities and accuracy were reviewed in detail recently in a comprehensive work by Thomas et al. (2017). Therefore, we will just summarize briefly the underlying physics that control the measurements. To perform velocity measurements, successive pairs of acoustic wave pulses separated by a time interval Δt (ping interval) are emitted by the central transducer at a 'pulse-repetition-frequency' and scattered back by the acoustic tracers suspended in water to be detected by the receivers. The phase shift between the emitted and the received signals is then

analyzed to provide estimates of the velocity of the scattering elements. Due to its geometrical configuration, the profiler measures the velocity component along the angle bisector delimited by the transmitter and each receiver beam. For a perfectly-manufactured instrument in which receivers 1 and 3 are aligned with the streamwise plane of the flow, the four-measured velocities are transformed into a Cartesian coordinate system, the longitudinal u and the first vertical w_1 velocity components being obtained from beam velocities 1 and 3 and the transverse v and the second vertical w_2 components from beam velocities 2 and 4 according to Eqs. (1):

$$\begin{aligned} u &= \frac{b_1 - b_3}{2\sin\alpha} \quad \text{and } w_1 = \frac{b_1 + b_3}{2\cos\alpha}, \\ v &= \frac{b_2 - b_4}{2\sin\alpha} \quad \text{and } w_2 = \frac{b_2 + b_4}{2\cos\alpha}. \end{aligned} \tag{1}$$

where b_i, with $i = 1$ to 4, are the beam velocities and α which varies around 15° along the measuring profile is the bisector angle between the transmitted and any received beams. In practice, the instrument configuration is not perfect and the transformation of beam velocities into Cartesian velocities involves a 4x4 matrix obtained by a manufacturer calibration and set up directly into the instrument software. However, from Eqs. (1), it is easy to see that the noise affecting velocity signals will be significantly larger on the longitudinal u and crosswise v components than the vertical ones, w_1 and w_2, the ratio of the respective variances varying typically as $\tan^{-2}\alpha$, i.e. in the magnitude range from c.a. 7 to 27.

As acoustic Doppler velocimeters are known to work poorly in clear water due to the low acoustic energy level backscattered to receivers, the quality of velocity data collected by these instruments is largely dependent on the quality and the density of the acoustic tracers present or introduced into the water flow (Blanckaert and Lemmin 2006; Thomas et al. 2017). Owing to the difficulties of seeding in bulk for a long period of time a volume of water as large as 100 m^3 without severe pollution due to particle sedimentation, the best method we found for seeding this flow

efficiently was to generate hydrogen microbubbles by electrolysis, as suggested by Blanckaert and Lemmin (2006). For generating a regular and reproducible population of tiny hydrogen bubbles at a well-controlled rate in water, we chose to use 0.1 mm thick copper wires for the cathode and a 4 mm diameter aluminum rod for the anode. The bubble flux was then adjusted by varying the DC voltage between the two electrodes (around 20 V). For these experiments, the seeding system was composed of two copper wires and one aluminum rod, 0.56 m long in the transverse direction and 5 and 30 mm apart in the vertical direction (Figs.1b-c). The electrodes were fixed horizontally at the front of a frame by means of two vertical insulating stems, 0.1 m long, and the frame itself was set up on a vertical displacement system to adjust the wire depth for each flow condition. Note that during these experiments, this frame did not cause significant disturbances of the surface flow because it was generally immersed in the return flow which develops below the surface drift current but in the opposite direction and the 12 cm long vertical stems were located 0.28 m crosswise on either side of the sensor head (Fig.1c). In addition, to avoid as far as possible bubble buoyancy-induced disturbances inside the water surface boundary layer at the measuring section, but keeping mostly a homogeneous distribution of bubbles within this layer, the seeding system was placed at a distance of about 0.1 m upstream of the sample velocity profile. We will discuss more extensively the behavior of these tiny bubbles as passive flow tracers hereafter because it was found to be strongly dependent on wave and turbulence conditions. Note that the localized bubble seeding of the uppermost water layer enables visualization of the flow and thus provides a first overview of its main turbulent features. However, this seeding set-up does not allow simultaneous measurement of the velocity field in the return current.

3. Test Measurements

As pointed by many authors (see for instance Rusello and Allard (2012); Koca et al. (2017)), to perform measurements in the immediate vicinity of a solid wall or an interface by means of an acoustic Doppler velocimeter raises specific difficulties caused by the acoustic wave reflections at these boundaries. Therefore, before investigating more complex water flow dynamics as the wind-induced surface flow, the ability of the profiler to measure velocity fields in the thin layer just beneath the water surface has been examined in detail. To better assess the quality and the accuracy of the velocity data collected in this layer, preliminary tests were performed for a steady flow generated by two recirculating water pumps. For these tests, the profiler sensor was placed on the centerline of the large wind-wave tank at 28 m fetch. The transceiver was fixed vertically at a distance of 6.8 cm from the water surface at rest, as measured by the bottom check facility of the profiler just before the experiments, and the seeding system was immersed 0.10 m upstream with the upper wire at a distance of 2 cm from the surface. Velocity profiles were sampled over 30 levels with 1 mm high measuring cells. As recommended by the manufacturer, the *adaptive once* ping interval mode was used, the velocity range and the power level being adjusted at 0.1 m s^{-1} and *'High-'* setting values, respectively. For each measuring condition, time sequences of 240 s were recorded at a sampling frequency of 30 Hz. The statistical analysis of flow properties was performed on raw velocity data, the Goring and Nikora (2002) phase-space thresholding method for detecting spikes revealing that those represent less than 1% of the collected data in test experiments. Furthermore, this method is not applicable for flows oscillating randomly as observed just beneath a wavy air-water interface.

To illustrate these measurements, the instantaneous profiles of the four measured velocity components are displayed in a space-time representation during 8 s in Figs. 2b-e. The velocity values

are given by a color code and referenced to a right-handed Cartesian coordinate system with the longitudinal x axis oriented downstream and the vertical z axis toward the water surface. In addition, the beam-averaged acoustic power backscattered to the receivers is plotted in Fig. 2a in a similar representation. Acoustic power will be used in this work for evaluating the data quality rather than signal-to-noise ratio (SNR), both quantities being linked by a linear relationship (Thomas et al. 2017). For this flow, in the absence of well-developed small-scale turbulence, Fig. 2a shows that the seeding bubbles are carried by the fluid at the location of the profiler over about a 1.5 cm thick layer in which the acoustic power is very high, of the order of -20 to -10 dB. On both sides of this layer, the acoustic power drops drastically owing to the combined effects in the decrease of the scattering particle density in water and the decrease in the scattering volume as analyzed in detail in Brand et al. (2016) and Thomas et al. (2017). Very close to the water surface, the high power values observed should be ascribed to the strong acoustic wave reflection occurring at this boundary. Otherwise, the instantaneous streamwise velocity profiles observed in the sample layer (Fig. 2b) are rather flat, with values of the order of 8 cm s^{-1}, except in the region very close to the water surface where velocity vanishes. The spanwise velocity profiles present most of the time values around zero. These profiles also exhibit large-scale velocity fluctuations, typically of 1 to 2 cm s^{-1}, due very likely to persistent vortices generated by the pumps and advecting downstream without significant damping. The w_1 and w_2 vertical velocity profiles are estimated independently from bubble echoes backscattered in the longitudinal and transverse vertical planes respectively. These profiles are very similar, displaying values close to zero. In the upper levels however, positive values up to 1 cm s^{-1} can be observed. This small vertical velocity gradient may come from a slight buoyancy force acting on bubbles, in particular on the largest ones.

The properties of the acoustic return signals and the velocity field averaged over the whole time sequence are presented in Fig. 3. Fig. 3a shows the mean profiles of the acoustic power (also called

amplitude) scattered to the four receivers versus the distance h_t to the central transducer. These profiles vary very similarly, except that the beam 1 amplitude is 10 to 15 dB lower than the other three. The various results obtained here, in particular the fact that the beam 1 variation with depth matches the other variations, suggest this distinct behavior is very likely due to a lower response of the receiver 1 electronics rather than a receiver misalignment. Accordingly, phase measurements made by this device will be more sensitive to noise. Otherwise, the beam amplitude profiles exhibit the same typical shape, with a maximum at a level of c.a. 5 cm. This region is generally associated with the *sweet spot* for which the overlap between the transducer and receiver beams is optimal (Brand et al. 2016; Thomas et al. 2017). On both sides of the maximum, the beam amplitude decreases regularly but more rapidly in the layer above owing to the decrease of the bubble density at these flow levels. This decrease in bubble density also shifts the location of the amplitude maximum to a distance of 4.9 cm from the emitter rather than 5.0 to 5.2 cm as normally expected owing to the sensor geometry (i.e. around cells 10 to 12). Except for receiver 1, the average strength of the return signals scattered by bubbles remains very high, above -30 dB, thus indicating the satisfactory seeding quality (note that for all beams, a -30 dB amplitude value corresponds roughly to a 30 dB SNR). In the subsurface layer above 6.5 cm, the four beam amplitudes increase drastically due to contamination of the receiver signals by acoustic wave reflections from the water surface. The power maxima observed at the 6.87 cm level coincides very well, i.e. within the 1 mm profiler cell resolution, with the height of the water surface at rest as indicated by a dashed line in the graph. For such water flows with a flat air-water interface, the depth of the region contaminated by the surface echo is thus estimated at c.a. 4 mm (i.e. the depth including the first three cells just below the water surface).

The high quality of the seeding obtained when using electrolysis hydrogen bubbles is also illustrated by the high values of the correlation coefficients observed in the surface layer, as seen in

Fig. 3b. Except for beam 1, these values are higher than 97%, barely varying with height. The variations of the correlation coefficient on both sides of the sweet spot are much more pronounced for beam 1, owing to the weak return signal amplitude, but the observed values remain within the generally acceptable magnitude range for accurate velocity measurements, i.e. above 90% (Rusello and Allard 2012).

The vertical variation of the four mean flow velocity components measured by the Vectrino profiler is given in Fig. 3c. The mean streamwise velocity observed within the surface layer is constant except in the region contaminated by the surface echo. There, the measured velocity drops nearly to zero. The velocity values observed below oscillate slightly with depth around a value of 7.9 cm s^{-1} but are in a very good agreement with the average velocity estimated from the small float displacements at the water surface recorded by the camera. As the air-water interface is approached, pulse-to-pulse phase measurements and hence velocity values are affected by surface echo. This is corroborated by the observed trend of the beam 1 amplitude (or correlation) with transducer distance, its decrease comes to a halt at a depth of 3.9 mm and then reverses. Otherwise, as expected for a sensor well aligned with the longitudinal flume axis, the mean spanwise velocity wavers slightly with depth around zero, reaching at most ± 0.5 mm s^{-1}. Both estimates of the mean vertical velocity vary with depth in the same way, from small negative values (less than 1 mm s^{-1}) at the bottom of the sample layer to more significant positive values, up to 3.5 mm s^{-1}, close to the water surface. This variation may result from buoyancy effects dependent on bubble size distribution, the largest bubbles being preferentially conveyed at the highest levels. Note that spurious vertical and spanwise velocity measurements are also obtained in the subsurface layer when the acoustic backscattered power from bubbles is contaminated by surface echo. Hereafter, we will discard all velocity measurements within this c.a. 4.0 mm deep layer.

To evaluate the performance of the profiler for investigating the turbulent flow structure, the vertical variations of velocity variances are presented in Fig. 3d. Despite the fact that the instrument does not satisfy all the assumptions required for this evaluation, in particular the condition of isotropy owing to the lower value of the beam 1 amplitude, the method proposed by Hurther and Lemmin (2001) has been used to provide a rough estimate of the noise variance affecting each velocity component, as shown in Fig. 3e. Such estimates can be made because for evaluating the velocity field in a given plane, the contribution of the beam velocities from the other transverse plane remains small. So, as a first approximation, we can assume that the respective noises associated with both measured vertical velocities are not correlated. This method provides here only an order of magnitude estimate of noise variances. We should point out that the more elaborate method proposed recently by Thomas et al. (2017) modifies only marginally estimates of these quantities, very likely because the sensor does not fulfil the condition of noise isotropy between beam 1 and beam 3 required for applying it.

As seen in Fig. 3d, the longitudinal velocity variance $< u'^2 >$ exhibits a variation with height typical of highly noisy ADVP measurements (Blanckaert and Lemmin 2006). In fact, this quantity remains almost constant, of the order 0.5 cm^2 s^{-2}, in the region centered at the sweet spot around 5 cm, but increases considerably on both sides of the sampled layer, reaching at such levels values higher than 1 cm^2 s^{-2}. Thus, this profile appears largely controlled by the noise variance dependency on sensor distance (Fig. 3e). Compared to the longitudinal component, the transverse velocity variance profile presents a more expected shape for this type of turbulent flow, the observed velocity fluctuations keeping a constant intensity throughout the surface layer free from contamination by surface echo. Nevertheless, one can note that $< v'^2 >$ increases a little, up to 30%, for heights corresponding to the deepest measuring cells of the profiler, without any significant increase in the noise variance there (Fig. 3e). The noise variance contributes only 10

to 20 % to $< v'^2 >$ at all depths. Both estimates of the vertical velocity variance $< w_1'^2 >$ and $< w_2'^2 >$ as well as their normally noise-free covariance $< w_1' w_2' >$ are very low as expected for a flow developing below a horizontal surface. Their respective values do not exceed 0.1 $\mathrm{cm}^2.\mathrm{s}^{-2}$ and vary with height very similarly. The profiles exhibit a parabolic-like shape, $< w_2'^2 >$ and $< w_1' w_2' >$ following practically the same curve but $< w_1'^2 >$ varying with depth with a much more pronounced curvature. Consistently, the estimated $< w_2'^2 >$ noise variance is almost constant over the whole boundary layer, with values of less than 15% of $< w_1' w_2' >$ while that of w_1' fits a highly symmetrical parabolic-like curve, reaching values from 30 to 90% of $< w_1' w_2' >$.

To get a better idea of the origin of the noise, time series and frequency spectra of the velocity signals are displayed in Fig. 4 and Fig. 5 for three heights, one close to the sweet spot at $h_t = 5.2$ cm and the two others at the edges of the sampled layer, i.e. at $h_t = 4.1$ cm and 6.35 cm. In Fig. 5, we also report the normally noise-free cospectrum of both vertical velocity records w_1 and w_2. The spectra are computed using the classical Welch method over successive time-series segments of 2048 data points weighted by a Hanning window of same length with an overlap of 1024 points. At the sweet spot, the vertical velocity signals vary with time in the same way, exhibiting only tiny fluctuations at high frequencies, and sporadically more significant spikes (Fig. 4). The w_2 spectrum and the $w_1 w_2$ cospectrum almost collapse into the same curve, except at frequencies above 3 Hz where w_2 spikes may contribute to higher w_2 spectral levels (Fig. 5). The w_1 spectrum deviates from that of w_2 but to a lesser extent, being slightly higher at all frequencies. The u and v time records first exhibit large-scale fluctuations clearly visible in both signals and most likely associated with turbulent flow vortices. At high frequencies however, they display much more random fluctuations than vertical velocity signals. In fact, the ratio of the horizontal and vertical velocity spectra above 10 Hz agrees well with the ratio of the related beam geometrical coefficients

at the sweet spot (i.e. 14, see Eqs.(1)). This indicates that noise fluctuations rather than turbulent motions dominates the spectral energy densities in this frequency range.

In Figs. 4b-c, the velocity signals observed at the edges of the sampling layer are undoubtedly much noisier, displaying much wider fluctuations at high frequencies. Accordingly, below 1 Hz, longitudinal and transverse velocity spectra match quite well those observed at the sweet spot (i.e. within the confidence interval) but beyond this frequency, they exhibit much higher levels, in particular the longitudinal component at the nearest height above the transducer (up to a factor 10). Conversely, the vertical velocity spectra differ from those observed at the sweet spot for all frequencies, and this is more noticeable at low frequencies at the deeper level ($h_t = 4.1$ cm) but above 1 Hz at the upper level ($h_t = 6.35$ cm).

Fig. 3f presents the variations with height of velocity variances corrected from noise by two different methods: i) by using the Hurther and Lemmin (2001) method as discussed above (continuous lines), ii) by summing velocity spectra at low frequencies, up to a cut-off of 1 Hz (dotted lines), following Brand et al. (2016). This figure reveals that for this low-turbulence flow, the second method provides much better results. One can see that $< u'^2 >$ and $< v'^2 >$ are constant and of similar magnitude, typically 0.35 cm^2 s^{-2}, over the whole measuring layer. The filtering method appears less efficient for correcting vertical velocity variances from noise, $< w'^2_{1,2} >$ still exhibiting a minimum at the sweet spot and increasing values on both sides of this region. This increase is however stronger at the bottom levels of the surface layer than at the upper levels, suggesting a different origin from only a beam decorrelation which affects Reynolds stress estimates (Brand et al. 2016). As expected, the Hurther and Lemmin (2001) method provides rather poor results for the profiler used in this experiment. It appears that this noise correction on $< u'^2 >$ is overestimated at the largest distances from the transducer but underestimated at the lowest ones, giving accurate results only in the sweet spot region around 5.2 cm. In addition, this method does

not improve estimates of the spanwise velocity variance at the lower heights below 4.5 cm. In essence, according to the underlying assumptions of the method, both vertical velocity variance estimates should collapse into the supposed noise-free $< w'_1 w'_2 >$ covariance. If the values observed for this quantity at the sweet spot seem to be in good agreement with those obtained by filtering, the $< w'^2_{1,2} >$ estimates outside this region look strongly affected by noise, or perhaps by other instrument defects. In fact, the analysis of velocity field properties performed above clearly shows that velocity measurements made by the Vectrino profiler used here are much more prone to noise contamination owing to the low level of the beam 1 amplitude but also it indicates that these measurements may suffer from minor calibration errors, in particular at low distances from the transducer. Below the sweet spot, it appears indeed that velocity measurements in the transverse plane are contaminated by the flow velocity field in the longitudinal plane. Similar anomalies have been detected previously by several authors, such as Zedel and Hay (2011), and a new calibration procedure was proposed by Nortek in 2016. However, the Vectrino profiler software used in the experiments carried out in 2014 does not take into account this new algorithm.

4. Observations of the wind-driven subsurface water flow

The potential of the Vectrino profiler for investigating the dynamical properties of the wind-driven near-surface water boundary layer have been examined in a series of experiments where the velocity field inside the subsurface flow was measured at different stages of wind wave development. The observations were conducted at two wind speeds U (4.5 and 5.5 m s^{-1}) and eleven fetches X ranging from 1 to 15 m, i.e. for wind wave fields of wave height not exceeding 30 mm.

The overall arrangement of the instrumentation adopted for these experiments was the same as described in Sect. 2. The depth of the electrolysis wires and the profiler head was adjusted for each wind and wave condition to get the best bubble seeding within the sample layer and the longest

velocity profile below the highest wave crests observed. Thus, the depth of the upper electrolysis wire was kept between 1 and 3 cm and the sensor head was always immersed at a depth greater than 4.0 cm below wave troughs. The velocity range and the acoustic power level of the Vectrino profiler were set at 0.1 m s^{-1} and *'High-'*. For each forcing condition, the velocity profiles were recorded simultaneously with wave height and wave slope signals during three time sequences of 5 min separated by a time interval of 2 to 5 min. Wave signals were digitized at 256 Hz frequency while the sampling rate for velocity profile records was set at 30 Hz. These records were made after a minimum time period of 30 to 45 min necessary for stabilizing the water flow within the tank after a change in wind or fetch conditions.

a. Wind waves observed at the water surface

Before analyzing the velocity field generated by wind and waves in water, we describe wind wave properties observed at fetches and wind speeds selected for these experiments. Typical time series and spectra of wave height and wave slope observed at 4.5 m s^{-1} wind speed are shown in Figs. 6a-d for several fetches. In addition, the fetch dependence of a few related statistical wave parameters is given in Figs. 6e-h. At the first fetch upstream, the water surface looks practically flat with only tiny oscillations observed in two distinct frequency ranges (6a-b). Wave motions around 3 Hz correspond to the small transverse oscillations of the water surface detected at the entrance of the tank, while those around 10 Hz, well-discernible only in the slope spectrum, correspond to the first wind-generated waves. Immediately downstream, Fig. 6a shows that wind waves grow approximately at the same frequency up to 3 m fetch, and a wide dominant peak is emerging from noise at around 10 Hz. In parallel, waves of higher frequencies start to develop, very likely associated with dominant wave harmonics. The dominant waves clearly display nonlinear shape with round crests and sharp troughs and are arranged in three-dimensional surface patterns (see Fig.2 in

Caulliez and Collard (1999)). Beyond 3 m fetch, the dominant peak keeps growing significantly in energy but with a regular shift towards lower frequencies while a saturation range develops at frequencies higher than 20 Hz. The formation of this saturation range results from the rapid development of parasitic capillary ripples propagating at the front of the highest dominant wave crests, as seen in Fig. 6c-d. The wave slope spectra displayed in Fig. 6b exhibit the same variation with fetch, except that the spectra contain proportionally more energy at high frequencies. At this wind speed, the dominant wave height increases from a few tenths of a millimeter for fetches below 3 m to about one centimeter at 15 m fetch, as seen in Fig. 6c or better quantified in Fig. 6e using the variation with fetch of the RMS wave amplitude. In addition, Fig. 6g shows that dominant waves keep roughly the same wavelength up to 4 m fetch, typically 4 cm at 4.5 m s^{-1}, but downstream, this quantity increases gradually up to 15 cm. The nonlinear shape and the related dynamic properties of dominant waves thus shift from capillary-gravity to short gravity wave types. The wave slope spectra enable us to evaluate separately the total mean square slope (*mss*) associated with dominant waves and small-scale wave roughness, respectively. The former has been estimated by spectrum integration from 0.5 to 1.5 times the dominant peak frequency f_d while the latter has been estimated by integration over a scale domain ranging above the smallest of both frequencies, namely 20 Hz and 3.1 times f_d. The variation with fetch of the average dominant wave steepness (i.e. the square root of the dominant wave *mss* denoted ak_d for simplicity) and the small-scale wave *mss* thus estimated are displayed in Figs. 6f-h. We see that ak_d first increases regularly but slowly at fetches lower than 3 m whereas downstream, the growth accelerates significantly up to 6 m. Beyond this fetch, the growth slows down drastically, ak_d becoming almost constant, then rating 0.14 for 4.5 m s^{-1} wind speed. In parallel, the short wave *mss*, mss_{eq}, being negligible at the first fetches, starts to grow rapidly beyond 3 m to reach a maximum at 6 m. Downstream, this quantity decreases slowly to a fetch of 8 m beyond which a plateau is observed, amounting

to c.a. 5×10^{-3}. The changes with fetch in wave height and slope spectra and the related wave parameters observed at 5.5 m s^{-1} wind speed are very similar, except that they are much faster, the rapid growth of ak_d and mss_{eq} starting at 1.5 m fetch, both quantities then reaching equilibrium values around 8 m but with a mss_{eq} overshoot located at c.a. 3 m.

b. Detection of surface motions by the profiler

A major difficulty when performing single point velocity measurements in the immediate proximity of a wavy surface is the lack of precise estimate of the instantaneous location of the velocity sample collected with respect to the surface. This distance to the surface is required for reconstructing in an appropriate way the vertical variation of the averaged properties of the various water flow motions, namely the mean wind-induced drift current, the wave-induced orbital motions and the turbulent motions. In fact, as pointed out in Caulliez (1987), averaging over time measurements made at a fixed Eulerian location in such a shear flow introduces significant bias in estimates of the flow characteristics because the variation in time of the actual depth and the orbital motions are linked in phase. As first noted in Section 3, the Vectrino profiler offers the possibility of retrieving the instantaneous measuring depth when the water surface is embedded in the sampled layer. Accordingly, this knowledge of the colocalized motion of the water surface enables us to reconstruct the velocity field below waves in a curvilinear reference system in which orbital motions do not contribute to the mean flow and vice versa, at least at the first order.

Fig.7a presents a time sequence of the vertical profiles of the beam-averaged acoustic power backscattered to the receivers when wind waves are well-developed at the water surface. The z axis origin refers to the water level at rest as measured by the profiler bottom check, i.e a distance of 62 mm from the transceiver. As for the flat-surface channel flow investigated previously in Section 3, the very high acoustic power observed at the water surface (> -5 dB) compared to

the acoustic power backscattered by hydrogen bubbles advected by the flow makes this boundary clearly distinguishable. Here again, this phenomenon is due to the high acoustic wave reflection occurring at the air-water interface. Consistently, taking advantage of this observation, we have developed an algorithm to determine with a resolution of 1 mm the water surface elevation associated with each sampled velocity profile. The procedure is based on the detection of the backscattered acoustic power field maxima. First, each instantaneous acoustic power profile is filtered from noise by applying a smoothing window 3 pixels in height. The maximum of the profile at a given time is then detected from the location of the previous one by searching it within a limited height interval, the latter being estimated as the largest surface wave displacement observed by the capacitance gauge located just downstream from the sensor. To illustrate this procedure, the time sequence of the surface elevation associated with acoustic power maxima observed in Fig.7a is shown in Fig.7b.

This method for retrieving the instantaneous water surface elevation at the location of the profiler was validated by comparing the corresponding wave spectrum with that derived from wave probe records. To facilitate the comparison, the wave probe signal was resampled in time at the nearest frequency of the velocity data acquisition rate, i.e. 32 Hz, and in height with a 1 mm resolution. Fig. 7c shows that both wave height spectra overlap very well over the dominant peak centered around 5.8 Hz, the estimates of associated RMS dominant wave amplitude differ by less than 1 %. However, the wave spectrum derived from acoustic detection contains higher noise at all frequencies which precludes the detection of higher wave harmonics. This background noise results undoubtedly from the low resolution in height of the wave signal and the lack of high frequency filtering.

Using these colocalized wave height measurements and assuming as a first approximation that the orbital motions of dominant waves satisfy the linear wave theory, the velocity field in the upper

near-surface layer and its statistical flow properties will be described hereafter along the dominant wave streamlines centered at a distance z from the mean surface level, i.e. along the vertical coordinate $\tilde{z}$ given by the equation:

$$\tilde{z}(z,t) = z + \eta(t) \cdot e^{kz}, \tag{2}$$

in which $\eta(t)$ is the instantaneous vertical displacement of the water surface estimated at the location of the profiler and k, the dominant wavenumber derived from the measured dominant wave frequency f_d and phase speed c_d.

c. Mean subsurface flow observed in water

Figs. 8a-b present the vertical distribution of the mean longitudinal velocity as observed in the wind-generated boundary layer just beneath the water surface for all fetches and both wind speeds. When waves ruffle the water surface, these time-averaged velocity profiles are estimated by using the curvilinear coordinate system introduced above. The velocity is then averaged along the dominant wave streamlines $\tilde{z}$ centered at a distance z from the mean surface level. To determine the average flow properties from high quality velocity data, sequences of velocity signals for which the acoustic power is higher than -30 dB during a time interval of at least 512 successive points have been selected and then, time-averaged quantities have been computed for the whole selection. In addition, in Figs. 8a-b, velocity data obtained in the uppermost 3.5 mm thick sublayer have been discarded from the profiles (except for the first one as illustration) because there, the acoustic power backscattered by bubbles to the receivers is contaminated by the water surface echo, as analyzed in detail in Sect. 3.

The mean values of the surface drift current are also reported in Figs. 8a-b. They are estimated using PTV with an interpolation at the appropriate fetch. To better appraise the spatial development

of the water boundary layer, the variation with fetch of the mean flow velocity observed at the surface and at 10 mm depth is shown in Figs. 8c-d.

As marked by three different symbols, the vertical distribution of the mean velocity exhibits three distinct behaviors when the boundary layer develops spatially under wind forcing. At the entrance to the water tank, when the water surface is still flat, the flow is confined in a thin layer of about 15 mm depth. There, in absence of waves, the formation of the boundary layer results only from the direct action of the air viscous stress exerted by wind at the interface and the viscous diffusion of the longitudinal momentum downward throughout the fluid. Although the profiler does not enable investigation of the upper part of the flow, we can assume, given the high velocity values observed at the surface, that the rapid decrease of the mean velocity is likely to be linear in the uppermost millimeters of the boundary layer, as shown previously in Caulliez et al. (2007) from a detailed laser Doppler velocimeter (LDV) investigation performed in a smaller tank. Below this highly-sheared sublayer, the mean flow decreases much more slowly at a progressively falling rate towards the lower edge of the boundary layer. Note that the depth where the mean velocity vanishes or even reverses due to the development of a return current in the flume cannot be determined precisely when local particle seeding is used. For this experimental arrangement, ADVP measurements can be made only when tracers move towards the sensor, i.e. for a flow in the wind direction but not for a vanishing-speed or reverse flow. During this laminar stage of flow development, the mean velocity gradually increases with fetch over the entire boundary layer. As shown in Figs. 8c-d at the shortest fetches, these measurements confirm rather well that the surface velocity varies with fetch according to a power law $X^{1/3}$ as expected for a viscous boundary layer accelerated at the surface by a constant wind stress (Caulliez et al. 2007).

When waves start to grow more rapidly at the water surface, i.e. at 4 and 5 m fetches for 4.5 m s^{-1} wind speed (Fig. 6e-f) and at 2.0 and 2.5 m for 5.5 m s^{-1}, the shape of the mean ve-

locity profiles changes dramatically compared to those observed previously at the laminar stage of the boundary layer formation. The mean surface drift velocity drops by about 30 % whereas the boundary layer deepens sharply, significant velocity values being observed at all depths of the measured profiles. This behavior suggests that the boundary layer undergoes an abrupt laminar-turbulent transition. The onset of this phenomenon can also be detected by the high variability of the surface drifter motion observed in this region, as indicated by the large error bars plotted in Figs. 8c-d or checked qualitatively by viewing the recorded microbubble images. This phenomenon will be analyzed on a more quantitative basis hereafter, by investigating the turbulent flow properties. Note that the inflectional profile observed at 2 m fetch for 5.5 m s^{-1} wind speed reveals that the boundary layer at this stage of transition is highly unstable.

Further downstream, at fetches up to $X = 8$ m, the velocities of the surface drift current and the bulk flow increase again by 1 to 3 cm s^{-1} at 4.5 m s^{-1} or a few millimeters per second at 5.5 m s^{-1}. The most striking feature of both flows at this stage of development is that the profiles are very flat, which indicates strong vertical mixing within the boundary layer. Hence, it seems difficult to identify a region where the profiles follow a logarithmic decrease with depth, as expected for turbulent boundary layers along a moving rigid wall. For both wind speeds, the best agreement with such a law would occur between 5 and 12 mm depth but the corresponding values of the friction velocity $u*_w$, practically invariant with fetch, prove to be very low, roughly 30 to 40 % of the values estimated from the measured friction velocities in air $u*_a$ when Reynolds stress continuity is assumed across the air-water interface. At the bottom of the sample boundary layer, i.e. below 20 mm depth, most of the profiles exhibit a small increase in velocity. This behavior is probably due to measurement errors introduced by the Vectrino profiler at the first levels above the sensor owing to calibration defects, as previously detected in Sect. 3. Finally, beyond 8 m fetch for both wind speeds, the variation with fetch of the mean flow velocity observed at all depths

including the water surface is characterized by a slow but well-identified decrease. However, the profile shape does not change significantly.

Note that the vertical velocity field measured in the boundary layer does not vanish on average, the hydrogen bubbles used as tracers being driven by slight buoyancy forces. The generally positive velocity values observed vary a little with depth, from 2 to 3.5 mm s^{-1} when the flow is laminar (i.e. values similar to those observed in Sect. 3) to less than 1 mm s^{-1} when intense turbulent motions develop at the longer fetches.

d. Fluctuating velocity field in water

To evaluate the performance of the profiler for investigating the spatial development of turbulent and wave motions inside the water boundary layer, frequency spectra of the three velocity component time series observed at 10 mm depth for all fetches are shown in Fig. 9 for 4.5 m s^{-1}. These spectra are computed from each time sequence of 512 points selected for estimating the mean flow profiles and then averaged, as explained above. Note that these individual time sequences are short enough to allow a high rate of data selection, i.e. generally between 60 and 100 % except for the two to three lower cells at the bottom of the sample layer where the bubble seeding is less regular. However, they are long enough (17 s) to capture most of the fluctuating motions of the flow except probably for the conditions for which the flow is highly nonhomogeneous, i.e. at fetches where the laminar-turbulent transition occurs or large-scale longitudinal vortices develop downstream. This will be described in detail later on. To minimize the noise contribution, the vertical velocity spectra are computed from the cospectra of both vertical velocity signals measured in the longitudinal and transverse planes respectively.

One can see in Fig. 9a that the vertical velocity spectra $S_{w_1w_2}$ exhibit two different trends associated with two frequency ranges and two types of water motions. At low frequencies, below

c.a. 1 Hz, $S_{w_1w_2}$ decreases regularly with frequency, first quite slowly up to 0.5 Hz, then a little more rapidly. The spectral level increase with fetch observed in this frequency range is due to the development of vertical turbulent motions in water. At frequencies above 1 to 2 Hz, the vertical velocity spectra show one or two well-marked peaks located at the same frequencies as those observed in wave spectra displayed in Fig. 6. Within this range, $S_{w_1w_2}$ appear to be largely dominated by the orbital motions of surface waves, their shape and their energy level changing with fetch in the same way as wave spectra. Consistently, the wide maximum observed around 2.5 Hz at fetches shorter than 3 m refers to transverse surface oscillations detected at the entrance of the water tank while the conspicuous peak that grows sharply with fetch with a shift towards low frequencies from 10 to 3.5 Hz, refers to wind-amplified dominant waves. However, the orbital motions associated with small-scale waves that contribute to the spectral energy saturation range are not clearly distinguishable in velocity spectra primarily because of the low rate of velocity sampling used here (30 Hz) but also due to the faster decrease of such motions with depth.

The streamwise and spanwise velocity spectra shown in Figs. 9b-c contain more energy than the vertical ones at frequencies below 1 Hz, their level being multiplied by a factor of 10 at fetches shorter than 3 m and a factor of 2 to 3 at longer fetches when turbulent motions develop. At the shortest fetches too, the streamwise velocity spectra above 1 Hz change in slope and start to level off at a spectral value of 1-3 $\times 10^{-3}$ cm^2 s^{-1}. This spectral floor may originate from small-scale velocity fluctuations which develop simultaneously with larger disturbances of laminar boundary layers or the first surface motions but also the profiler noise that is much higher for the u and v components than w (see Sect.3). As a consequence, the longitudinal orbital motions emerge from this background floor only at 3 m fetch. Downstream, at 4 m fetch, the orbital motions also barely emerge from the continuous spectral decay of highly-energetic turbulent motions which develop intensively at scales above 1 Hz following the laminar-turbulent boundary layer transition. Further

downstream, the spectral peaks associated with higher-amplitude dominant wave motions become clearly distinguishable, especially since the spectral level of turbulent motions decreases a little there. Nevertheless, the spectral dominant peaks observed for u contain noticeably less energy than those observed for w. The behavior of the spanwise velocity spectra look very similar to those of the streamwise component, except for two features. At low frequencies, the spanwise velocity fluctuations, being of the same order of magnitude as the streamwise ones at 0.1 Hz, decay much more slowly as frequency increases, the spectra remaining practically flat up to 1 Hz. At frequencies above 3 Hz, the peak of dominant wave motions can be clearly identified only for 15 m fetch. The ratio of the orbital motions in the spanwise direction to those in the streamwise direction then looks unexpectedly small, of the order of one tenth. When referred to the linear wave theory, this ratio should normally be comparable to the *mss* ratio observed for these dominant waves, i.e. of the order of 0.3. At fetches downstream 3 m, the spectral decay characteristic of turbulent flow motions at high frequencies thus can be detected almost to 10 Hz for the v component but the relatively high spectral level observed in this frequency range cannot explain the orbital velocity ratio discrepancy.

The variation with fetch of the three velocity component spectra below 1 Hz as observed in Fig. 9 reflects quite well the peculiar growth of turbulent motions in water at the subsurface flow laminar-turbulent transition. At the three shortest fetches, the spectral level of velocity fluctuations is very low, of the order of 10^{-2} cm^2 s^{-1} for u and v and 10^{-3} cm^2 s^{-1} for w. The significant increase of the velocity spectra observed at 2.5 and 3 m fetches indicates that stronger flow disturbances start to grow. The development of the first viscous shear flow instabilities is corroborated by visualizing the bubble images in which the formation of narrow elongated streaks can be clearly distinguished, as shown for instance in Fig. 10a. The surface flow laminar-turbulent transition primarily revealed at 4 m fetch by the sudden change in shape of the mean velocity profile (Fig. 8)

can also be detected in Fig. 9 from the drastic change of spectra both in shape and in energy. At 10 mm depth, the breakdown of the boundary layer is characterized by a rapid increase of the spectral energy density at low frequencies, the streamwise component reaching its highest level at 4 m fetch, typically 3 $cm^2\ s^{-1}$. Similarly, S_v and S_w reach high levels at low frequencies but more strikingly, at intermediate scales too, i.e. within the range from 0.5 to 5 Hz. This feature depicts undoubtedly the development within the flow of intense energy turbulent microstructures resulting from the breakdown of larger-scale streamwise vortices. Note that the ratio of S_w to S_u increases significantly during the transition, reflecting the enhancement of the vertical turbulent mixing. At 5 and 6 m fetches, the substantial decrease of velocity spectra at low to intermediate frequencies indicates that the generation of turbulent motions falls. This suggests that momentum transfer across the interface and throughout the subsurface shear layer is not high enough to maintain the turbulence production within the boundary layer at its highest level. However, the development of an inertial subrange at intermediate frequencies above 0.8 Hz as identified by the classical $-5/3$ power decay shows that a certain energy balance between turbulence production and dissipation processes tends to be reached at fine scales. Note too that the spectral level of spanwise velocity fluctuations remains the highest at all scales, a distinctive feature which highlights the specific nature of the wind-driven near-surface turbulent boundary layer. Finally, at fetches larger than 8 m, Fig. 9 shows that S_v and S_w increase again at low frequencies. These spectral changes may result from the growth of large-scale coherent streamwise vortices better known as Langmuir cells, as strongly suggested by the bubble trajectories visualized in the recorded images (Fig. 10b).

The vertical distributions of the standard deviations of the three velocity components associated with low frequency turbulent motions and dominant wave orbital motions observed for all fetches at 4.5 $m\ s^{-1}$ are shown in Figs. 11 and 12. These quantities are computed by spectral integration over respectively the low frequency range, from 0.05 to 1 Hz, and the dominant peak, from 0.5 to

1.5 times f_d. Like the mean velocity profiles, the RMS velocity profiles associated with turbulent fluctuations exhibit three distinctive shapes associated with the three stages of the boundary layer development. At fetches shorter than 3 m, when the flow is laminar, the turbulence intensities are quite small, of the order of or less than 2 mm s^{-1}, apart from the streamwise component at 2.5 and 3 m fetches. The increase occurring there at all depths reflects the growth of the longitudinal shear flow disturbances associated with the formation of viscous streaks aligned in the streamwise direction (Fig. 10a). The development of such coherent structures characterized by high-speed and low-speed regions randomly distributed in the spanwise direction makes the near-surface velocity field observed at a fixed location more and more variable due to the increasing nonhomogeneity of the flow. The viscous flow instabilities originate and grow in the highly-sheared subsurface layer, creating there the strongest velocity disturbances. This would explain the regular increase of $\sqrt{< u^2 >_{LF}}$ observed at the uppermost depths, the noise contribution below 1 Hz being small (see Sect. 3).

The most drastic change in the profiles of turbulence intensities occurs at 4 m fetch, following the laminar-turbulent transition of the near-surface flow. These quantities increase by a factor of 3 to 6, the largest growth being observed for the spanwise and vertical components at depths between -15 and -20 mm, i.e. just below the bottom of the laminar boundary layer observed upstream. The strong but localized high-speed fluid ejections from the subsurface region towards the bulk water associated with the breakdown of the boundary layer can give rise at these depths to very wide space and time velocity fluctuations. When approaching the surface, the turbulent fluctuations decrease slowly for the longitudinal component but more significantly for the vertical and transverse components. These variations can be explained when it is assumed firstly, that the less intense energy and small-scale flow disturbances remain confined within the uppermost region of the flow, and secondly, that the presence of the water surface prevents in this region flow

instabilities from growing in the upward direction, and thus in the spanwise direction too. Note again that at all depths, the turbulence intensity in the vertical direction is less than half that of the horizontal ones.

Consistent with the decrease of the mean flow at fetches immediately downstream of the laminar-turbulent transition, the turbulent velocity fluctuations noticeably decrease there too, as previously pointed out from the velocity spectrum variations. The drop, of the order of $1/3$, is particularly marked for the streamwise component at all depths. For the spanwise and vertical components, the drop is confined to the lower part of the sample layer. Thus, the variations with depth of such quantities greatly diminish, indicating that the structure of the turbulent flow tends to be more uniform and steady throughout the surface boundary layer. Unlike the mean flow which grows noticeably between 5 and 8 m fetches, the turbulence intensities at this stage of flow development remain remarkably constant, their variations with fetch being limited to c.a. 1 mm s^{-1} . At fetches larger than 8 m however, when the mean flow decreases again, the spanwise and vertical turbulence intensities start to grow significantly with fetch within most of the surface layer, except naturally the vertical intensity at the smallest depths. Instead, the streamwise turbulence intensity remains capped at the same level in the central part of the boundary layer. As suggested previously, this fluctuation behavior appears to be linked with the development of Langmuir cells within the surface flow.

To complete this analysis, in particular to assess the degree of confidence of turbulence intensity measurements close to the surface and at the bottom of the sample layer, complementary flow properties have been examined to appraise noise contamination, since the Hurther and Lemmin (2001) method cannot be used for the present anisotropic ADVP sensor. As discussed previously, the first criterion is based on the variation with depth of the backscattered acoustic power which enables determination of its trend reversal depth when approaching the surface, from a slow de-

crease to a fast increase. Secondly, the Doppler noise from two sampling cells being not correlated, the level of the spectral coherence between velocity records observed at two successive depths appears to be a good indicator for estimating noise contribution to velocity fluctuations of scales larger than one cell size. For fetches larger than 3 m, when the flow is fully turbulent, we thus found that the spectral coherence at frequencies lower than 1 Hz is always higher than 0.9 for the vertical component and 0.8 for the spanwise one, indicating that the contribution of noise to these turbulence intensities is rather weak. At short fetches, when the flow is laminar, the velocity fluctuations at low frequencies being much smaller, the spectral coherence drops to 0.6 or less, in particular at the uppermost depths, indicating that noise contributes much more significantly to the raw turbulence intensity estimates. For the streamwise component, the beam 1 acoustic power being quite low (see Sect. 3), the spectral coherence is generally weaker than for the two other velocity components, reaching values higher than 0.8 at frequencies up to c.a. 0.3 Hz but diminishing rapidly beyond. The decrease is particularly marked at the two smallest depths for fetches longer than 6 m for which outlier turbulence intensity values are observed. In fact, at fetches where wave height becomes significant, i.e. 1 cm typically, the minimum of the beam 1 acoustic power moves progressively from 3.5 to 5.5 mm depth. The streamwise velocity spectra observed in this region appear much noisier at all frequencies too. Therefore, these data are considered to be highly contaminated by noise and have been discarded from the streamwise turbulence intensity profiles (plotted just as symbols in Fig. 11).

The turbulence intensity profiles also present a few outlier data at the bottom of the sample layer, in particular for the streamwise component at 11 m fetch. The velocity measurements made at this fetch differ from the others by a low rate of selection of time sequences for which the averaged acoustic power remains above -30 dB. Below 18 mm depth, this rate decreases to less than 50 % due to a lack of bubble seeding. This very low percentage is linked undoubtedly to

the onset of Langmuir circulations and the formation of divergence zones in which fluid from the deep water rises upward without bubbles (see Fig. 10b). This phenomenon may introduce bias in measurements of averaged quantities as mean velocities or turbulence intensities, since the flow properties observed under such conditions are more representative of convergence zones characterized by downward motions than divergence zones characterized by water upwellings.

Fig. 13 displays the dependence on depth and fetch of the vertical turbulent momentum flux $< -u'w'_2 >$ estimated by integration of the longitudinal and vertical velocity cospectra from 0.05 to 1 Hz frequencies. Although the effects of beam decorrelation are certainly more pronounced, this covariance was chosen to estimate the vertical flux rather than $< -u'w'_1 >$ because its contamination by the Doppler noise proves to be lower for the instrument used here. Owing to the fact that the beam 1 and beam 3 acoustic powers and then the related noise variances differ widely, the noise variance should contribute significantly to $< -u'w'_1 >$ estimates (Brand et al. 2016). Fig. 13 confirms quite clearly the changes in fetch of the near-surface boundary layer structure described above in detail. During the laminar flow regime observed for fetches less than 3 m, $\sqrt{< u'w'_2 >}$ has insignificant values, thus corroborating the absence of vertical momentum transport by the weakly fluctuating velocity field observed at this stage of flow development. The sudden increase of the vertical Reynolds stress observed at 4 m fetch, in particular at the greater depths of the sample layer, attests that the breakdown of the surface boundary layer occurs there or more likely just upstream. The formation of large-scale turbulent eddies and the associated bursting events which characterizes this sharp by-pass transition to turbulence as described in Caulliez et al. (2007), is then responsible for strong downward advection of the streamwise momentum from the subsurface layer towards deeper flow regions. Consistent with the mean flow and turbulence intensity decrease with fetch, the vertical momentum flux also decreases drastically downstream of the laminar-turbulent transition but become practically invariant with depth and fetch. This suggests

724 that turbulent mixing throughout the surface boundary layer becomes homogeneous even if the
725 respective contribution to momentum transport from the viscous instabilities generated close to
726 the water surface and the large-scale Langmuir circulations may change, seeming specific to each
727 wind and wave field condition.

728 The vertical distribution of the RMS amplitude of dominant wave orbital motions estimated
729 from the three velocity spectra is given in Fig. 12 for 4.5 m s^{-1} and all fetches. The exponential
730 decrease with depth of the vertical RMS orbital velocity as derived from the RMS dominant wave
731 amplitude by using the linear wave theory is also plotted in Fig. 12c for fetches larger than 5 m
732 (dashed lines). This decrease is expressed by the following equation:

$$\sqrt{<\tilde{u}_{\mathrm{th}}>^2} = \sqrt{<\tilde{w}_{\mathrm{th}}>^2} = \sqrt{<\eta^2>}\, kc \cdot e^{kz} \tag{3}$$

733 First, Fig. 12 shows that the vertical component of the orbital motions decreases with depth and
734 increases regularly with fetch but the observed values deviate widely from those estimated by the
735 linear theory. However, as highlighted in Fig. 12d, the ratio of these quantities does not vary with
736 depth, keeping remarkably constant values in the layer where the vertical orbital velocity remains
737 significant (compared to noise or turbulent fluctuations), i.e. down to a depth of about 12 mm at
738 5 m fetch and 20 mm at 15 m fetch. This ratio also increases regularly with fetch, from roughly 0.6
739 at 5 m to 0.8 at 15 m. These findings indicate that the RMS values of the vertical orbital velocity
740 observed in this wind-driven sheared boundary layer decays exponentially with depth, following
741 a $\exp -kz$ trend with k being estimated from f_d and the measured phase speed c_d. Fig. 12d also
742 shows that the related amplitude can be approximated by $ak_d(c_d - U_s)$ rather than $ak_d c_d$ as derived
743 from Eq. (3), i.e. by removing the effect of the drift current on the measured phase speed as
744 predicted by the surface continuity equation. To support this outcome, further experimental but

also theoretical works are required because, to our knowledge, this basic question has not been solved for these specific shear flow conditions.

The variation with depth of the dominant wave orbital velocity in the streamwise direction, as shown in Fig. 12a, appears much more complex. At short fetches up to 8 m, $\sqrt{< u^2 >_d}$ decreases rapidly in the upper layer of the flow above 10 mm but below this depth, this quantity remains practically invariant, taking rather substantial values in particular at the first stages of the transition to turbulence at fetches just larger than 4 m. As previously detected in Fig. 9b, this trend corroborates the fact that quite intense turbulent motions develop at small scales above 5 Hz, thus contributing significantly to the fluctuating velocity field within the dominant wave spectral range. At fetches longer than 8 m, as orbital motions become dominant in the wave frequency range, $\sqrt{< u^2 >_d}$ varies with depth in a similar way as that of $\sqrt{< w^2 >_d}$ but only in the central part of the sample layer. When approaching the surface, the $\sqrt{< u^2 >_d}$ variation with depth differs dramatically, a drastic slowdown of the growth even leading to a trend reversal being observed. This unexpected behavior may result from the approximate reconstruction of the orbital velocity streamline depth from the linear theory because small errors in $\tilde{z}$ estimates could introduce large deviations in streamwise orbital velocity measurements. In this surface layer, owing to its high shear, these errors, even minute, may indeed affect directly average outputs obtained when the fluctuating velocity field is dissociated from the mean flow. The variation with depth of $\sqrt{< v^2 >_d}$ shown in Fig. 12b exhibits a similar behavior as the $\sqrt{< u^2 >_d}$ one. Note however that the respective weight of orbital to turbulent motions is noticeably lower in the spanwise direction, the near exponential decay being distinguishable only at fetches larger than 8 m. At 4 to 6 m fetches, the $\sqrt{< v^2 >_d}$ profiles then look quasi-flat since the contribution of small-scale spanwise turbulent fluctuations to $\sqrt{< v^2 >_d}$ proves to be largely dominant.

5. Concluding remarks

A series of tests and laboratory observations has been carried out in a large wind-wave tank to explore the potential of a multistatic Nortek Vectrino profiler for investigating the structure of the water boundary layer induced by wind and waves just beneath the surface. Compared to single-point velocimeters, such as LDV, this instrument has been found to have two major advantages. First, it can provide measurements of the three components of the velocity field along a short vertical segment within the surface sublayer. The available spatial and temporal resolutions, respectively 1 mm and 0.01 s, appears to be sufficiently high for such measurements, but the minimum distance to the surface to be reached for the data to remain valid is at best 3.5 to 4 mm, the data collected above are contaminated by surface echoes. Second, when embedded within the measuring profile, the water surface level can be detected simultaneously with the velocity field by tracking acoustic power profile maxima. Thus, it enables the determination of the instantaneous surface elevation with 1 mm accuracy and the instantaneous depth of velocity measurements. In future work, this feature may enable us to perform conditional analysis of turbulent structures with surface motions or wave groups and thus, to investigate in more details coupling between waves and water subsurface flow turbulence. However, the main difficulty in getting reliable velocity data, i.e. data weakly contaminated by noise, lies in the seeding quality. In the laboratory, when seeding of the bulk water is not easily feasible owing to the large size of the tank or the risk of pollution, hydrogen bubbles generated by electrolysis wires scatter a sufficiently high acoustic power to offer a good and cheap alternative to seeding particles. Simple methods have also been tested for appraising the signal quality and discarding velocity estimates contaminated by noise when seeding conditions were poor or intermittent, in particular, in immediate proximity to the surface

or the bottom of the boundary layer. These methods are particularly useful for investigations in which the Hurther and Lemmin (2001) method for removing noise is not applicable.

The velocity field inside the 2 cm thick water surface boundary layer driven by wind was explored along the first meters of the Marseille-Luminy wind wave tank. The spatial variation of the mean drift current profiles was described in a curvilinear coordinate system at the various stages of surface flow development. Thus, when fetch increases, we could identify the initial growth of the laminar water boundary layer driven by air surface wind stress, the development of viscous streaks, the abrupt laminar-turbulent transition, the coupled growth of orbital wave motions and finally, the formation of Langmuir cells. The characteristic scales and spatial growth rate of velocity fluctuations associated with the different types of motions have been described in detail. In particular, the RMS amplitude of the dominant wave orbital motions observed in such a highly-sheared subsurface boundary layer has been quantified. A few peculiarities of this turbulent boundary layer were also highlighted by comparison with those observed over a rigid wall. Among them, we report the noticeably high level of spanwise turbulent velocity disturbances relative to the streamwise ones.

This quite successful investigation of the wind-driven boundary layer by means of an ADV profiler also shows that further substantial measurement improvements can readily be made. Firstly, it is clear that measurement quality would be significantly improved by using an instrument with isotropic characteristics, enabling the diminution of data noise contamination and correction of the statistical flow properties from residual noise. Moreover, to improve water seeding, it would be of interest to design an array of electrolysis wires arranged upstream of the measuring profile and probably downstream too. Because the turbulent flow is characterized by very large upward and downward motions, such arrangement would enable investigation of the water flow dynamics throughout the surface layer in a more homogeneous way, and thus, the reduction of the potential bias introduced in averaging flow properties. In addition, to estimate properly the average flow

properties, this study clearly indicates the necessity of reconstructing the velocity field in a curvilinear coordinate system following the surface wave motion streamlines. Therefore, to improve the separation of the three foremost flow components contributing to the velocity field observed, i.e. the mean drift current, the dominant wave orbital motions and the turbulent fluctuations, a more robust and manageable model describing orbital motions within a highly-sheared flow should be developed. This knowledge would help to noticeably improve accuracy and reliability of various flow characteristics estimates, this enabling more extensive survey of the finescale dynamics of this very specific turbulent boundary layer.

Acknowledgments. The first author acknowledges the *Délégation Générale de l'Armement* and Aix-Marseille Université for funding his PhD fellowship. This work was supported in part by CNRS and CNES (DCT/SI/AR/2012-6324). The authors wish to express their special thanks to Nortek-MED in Toulon for the loan of the Vectrino-II instrument used for carrying these experiments. They are very grateful to Christopher Luneau for designing and constructing the experimental set-up and his technical assistance during the experiments, and to Victor Shrira for valuable comments on the results and suggestions regarding this manuscript. They also thank two anonymous reviewers for useful comments that improved the manuscript.

References

Banner, M., and W. Peirson, 1998: Tangential stress beneath wind-driven airwater interfaces. *J. Fluid Mech.*, **364**, 115145, doi:10.1017/S0022112098001128.

Blanckaert, K., and U. Lemmin, 2006: Means of noise reduction in acoustic turbulence measurements. *J. Hydraul. Res.*, **44 (1)**, 3–17, doi:10.1080/00221686.2006.9521657.

Brand, A., C. Noss, C. Dinkel, and M. Holzner, 2016: High-resolution measurements of turbulent flow close to the sediment-water interface using a bistatic acoustic profiler. *J. Atmos. Oceanic Technol.*, **33 (4)**, 769–788, doi:10.1175/JTECH-D-15-0152.1.

Brevis, W., Y. Nino, and G. Jirka, 2011: Integrating cross-correlation and relaxation algorithms for particle tracking velocimetry. *Exp. Fluids*, **50**, 135–147, doi:10.1007/s00348-010-0907-z.

Caulliez, G., 1987: Measuring the wind-induced water surface flow by laser doppler velocimetry. *Exp. Fluids*, **5 (3)**, 145–153, doi:https://doi.org/10.1007/BF00298454.

Caulliez, G., and F. Collard, 1999: Three-dimensional evolution of wind waves from gravity-capillary to short gravity range. *Eur. J. Mech. B/Fluids*, **18 (3)**, 389 – 402, doi:10.1016/S0997-7546(99)80036-3.

Caulliez, G., R. Dupont, and V. Shrira, 2007: Turbulence generation in the wind-driven subsurface water flow. *Transport at the Air-Sea Interface*, Springer, Berlin, Heidelberg, 103–117, doi:10.1007/978-3-540-36906-6_7.

Goring, D. G., and V. I. Nikora, 2002: Despiking acoustic doppler velocimeter data. *J. Hydraul. Eng.*, **128 (1)**, 117–126, doi:10.1061/(ASCE)0733-9429(2002)128:1(117).

Hurther, D., and U. Lemmin, 2001: A correction method for turbulence measurements with a 3d acoustic doppler velocity profiler. *J. Atmos. Oceanic Technol.*, **18**, 446–458, doi:10.1175/1520-0426(2001)018⟨0446:ACMFTM⟩2.0.CO;2.

Koca, K., C. Noss, C. Anlanger, A. Brand, and A. Lorke, 2017: Performance of the vectrino profiler at the sediment-water interface. *J. Hydraul. Res.*, **55 (4)**, 573–581, doi:10.1080/00221686.2016.1275049.

Lange, P., B. Jähne, J. Tschiersch, and I. Ilmberger, 1982: Comparison between an amplitude-measuring wire and a slope-measuring laser water wave gauge. *Rev. Sci. Instrum.*, **53**, 651–665, doi:10.1063/1.1137036.

Leng, X., and H. Chanson, 2017: Unsteady velocity profiling in bores and positive surges. *Flow Meas. Instrum.*, **54**, 136–145, doi:10.1016/j.flowmeasinst.2017.01.004.

Lhermitte, R., and R. Serafin, 1984: Pulse-to-pulse coherent doppler sonar signal processing techniques. *J. Atmos. Oceanic Technol.*, **1**, 293–208, doi:10.1175/1520-0426.

Nortek, 2013: Vectrino profiler, 3d profiling velocimeter. *Vectrino Profiler brochure*, Boston, MA, USA.

Peirson, W., and M. Banner, 2003: Aqueous surface layer flows induced by microscale breaking wind waves. *J. Fluid Mech.*, **479**, 138, doi:10.1017/S0022112002003336.

Rusello, P., and M. Allard, 2012: Near boundary measurements with a profiling acoustic doppler velocimeter. *Proc. 2012 Hydraulic Measurements and Experimental Methods*, Snowbird, UT, USA.

Rusello, P., A. Lohrmann, E. Siegel, and T. Maddux, 2006: Improvements in acoustic doppler velocimetry. *Proc. 7^{th} Int. Conf. on Hydroscience and Engineering*, Philadelphia, USA.

Siddiqui, M., M. Loewen, C. Richardson, W. Asher, and A. Jessup, 2001: Simultaneous particle image velocimetry and infrared imagery of microscale breaking waves. *Phys. Fluids*, **13 (7)**, 1891–1903, doi:10.1063/1.1375144.

Thais, L., and J. Magnaudet, 1996: Turbulent structure beneath surface gravity waves sheared by the wind. *J. Fluid Mech.*, **328**, 313344, doi:10.1017/S0022112096008749.

Thomas, R., L. Schindfessel, S. McLelland, S. Creelle, and T. D. Mulder, 2017: Bias in mean velocities and noise in variances and covariances measured using a multistatic acoustic profiler: the nortek vectrino profiler. *Meas. Sci. Technol.*, **28 (7)**, 075 302, doi:10.1088/1361-6501/aa7273.

Thomas, R. L., and S. McLelland, 2015: The impact of macroalgae on mean and turbulent flow fields. *J. Hydrodyn., Ser. B*, **27 (3)**, 427 – 435, doi:10.1016/S1001-6058(15)60500-5.

Veron, F., and W. Melville, 2001: Experiments on the stability and transition of wind-driven water surfaces. *J. Fluid Mech.*, **446**, 2565.

Zedel, L., and A. Hay, 2011: Turbulence measurements in a jet: comparing the vectrino and vectrino-II. *Proc. of IEEE/OES/CWTM 10th Working Conf. on Current, Waves and Turbulence Measurements*, 173–178, doi:10.1109/CWTM.2011.5759547.

LIST OF FIGURES

931 **Fig. 9.** Vertical (a), longitudinal (b) and spanwise (c) velocity spectra observed at depth $\tilde{z} =$
932 -10 mm for all fetches and 4.5 m s^{-1} wind speed. Line colors refer to fetches as indi-
933 cated in Fig. 8 legend box. The 90 % confidence interval of spectra is given at the top
934 left-hand side of the panel a). 51

935 **Fig. 10.** Views from above of three-dimensional water subsurface flow structures made visible by
936 electrolysis bubbles. a): Laminar streaks observed just before the breakdown to turbulence
937 of the wind-driven water boundary layer at 2 m fetch and 5 m/s wind speed. b): Langmuir
938 circulations observed at 13 m fetch and 4.0 m/s wind speed. The depth of the upper copper
939 electrolysis wire (visualized by the thick horizontal white line) is 3 and 2 cm respectively.
940 Wind blows from the bottom to the top of the images. 52

941 **Fig. 11.** Variation with dominant wave streamline depth $\tilde{z}$ of turbulence intensities estimated from
942 integration of velocity spectra at low frequencies (i.e. below 1 Hz) displayed for all fetches
943 (given in the legend box in meters) and 4.5 m s^{-1} wind speed: a): u', b): v', c): w'. 53

944 **Fig. 12.** (a)-(c): Variation with dominant wave streamline depth $\tilde{z}$ of the RMS values of the three
945 velocity components of dominant wave orbital motions as estimated from integration of
946 velocity spectra over the dominant peak, displayed for all fetches and 4.5 m s^{-1}: a): u,
947 b): v, c): w_2. d): Ratio between the measured RMS vertical orbital velocity value and this
948 estimated from measured surface motions by using the linear wave theory as plotted in (c)
949 by dashed lines. Color lines refer to fetches as given in meters in the legend box and the
950 dotted lines, to the respective ratios $ak_d(c_d - U_s)/ak_dc_d$. 54

951 **Fig. 13.** Variation with dominant wave streamline depth $\tilde{z}$ of the square root of the vertical momen-
952 tum flux $\sqrt{< u'w'_2 >}$ estimated from integration of velocity cospectra at low frequencies
953 (below 1 Hz), for all fetches and 4.5 m s^{-1} wind speed. Line colors refer to fetches as given
954 in meters in Fig. 11 legend box. 55

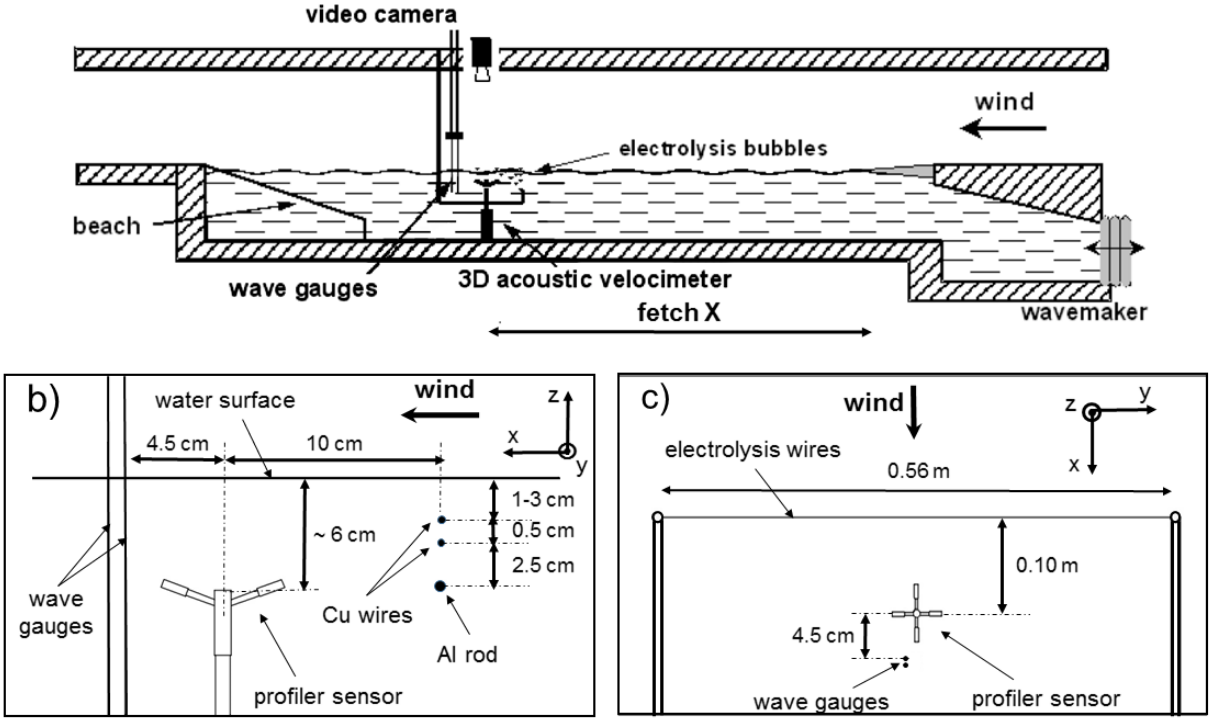

955 FIG. 1. Schematic diagrams showing (a) the facility and the general arrangement of the instrumentation set-up
956 . b): Enlarged side view showing the respective position of the profiler sensor, the electrolysis wires and the
957 capacitance wave gauges relative to the water surface at rest. c): Enlarged top view of the experimental set-up.

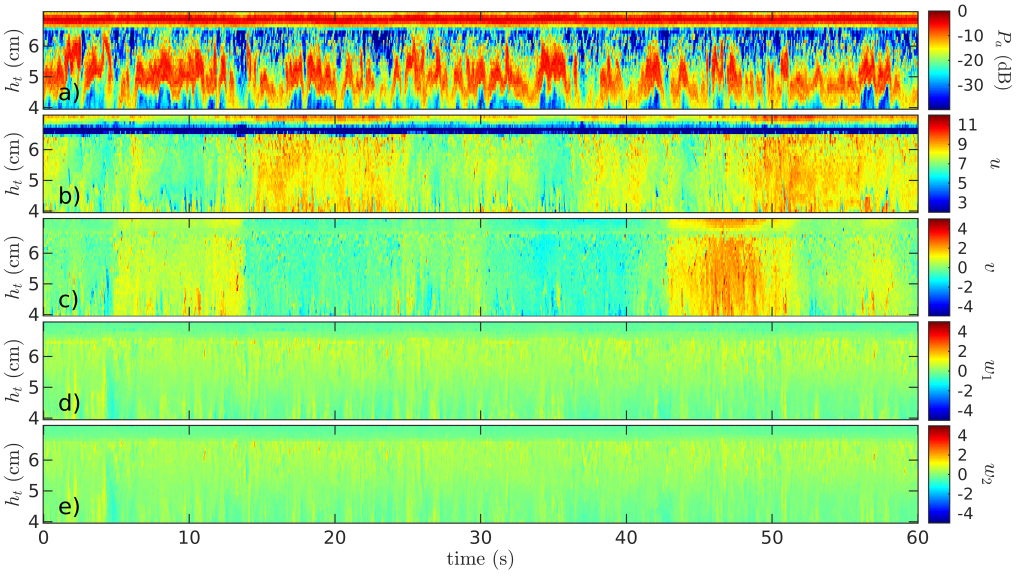

FIG. 2. Time variation of the vertical profiles of typical outputs of the profiler when observing the subsurface flow generated by recirculating pumps in the water tank: a) Beam-averaged backscattered acoustic power; b)-e) Flow velocity measured respectively in the longitudinal, spanwise and vertical direction (in cm s^{-1}).

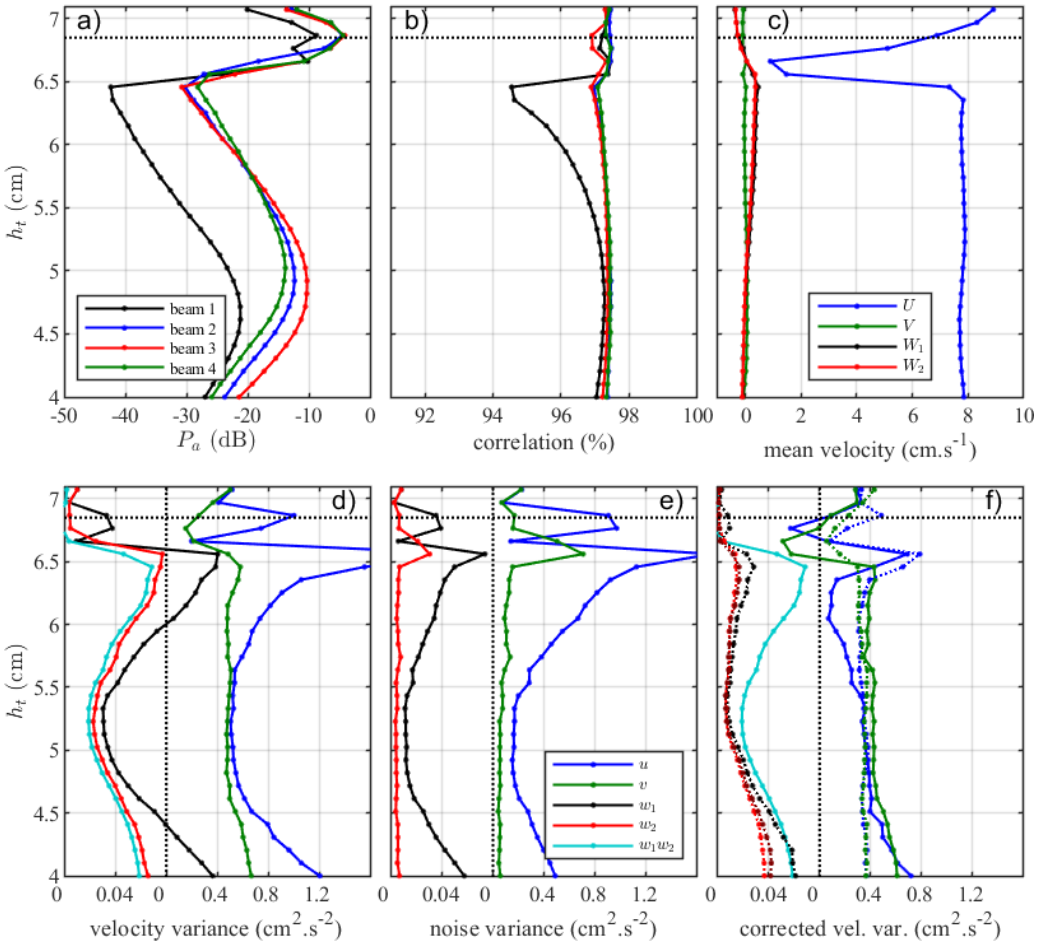

FIG. 3. Mean vertical profiles of various characteristics of the four acoustic beams backscattered to the ADVP receivers and statistical properties of the flow generated by recirculating pumps in the water tank: a) individual beam acoustic power; b) beam correlation; c) time-averaged flow velocity components; d) velocity variances; e) noise variances as estimated by the Hurther and Lemmin (2001) method; f) velocity variances corrected for noise by the Hurther and Lemmin (2001) method (solid line) and low-filtering method (dotted line). Line colors refer to the respective beam or velocity components as displayed in respective legend boxes. For readability, vertical velocity variance profiles in Figs. 3d-f are shifted from zero to the left and the corresponding x axis scale is zoomed in by a factor 10.

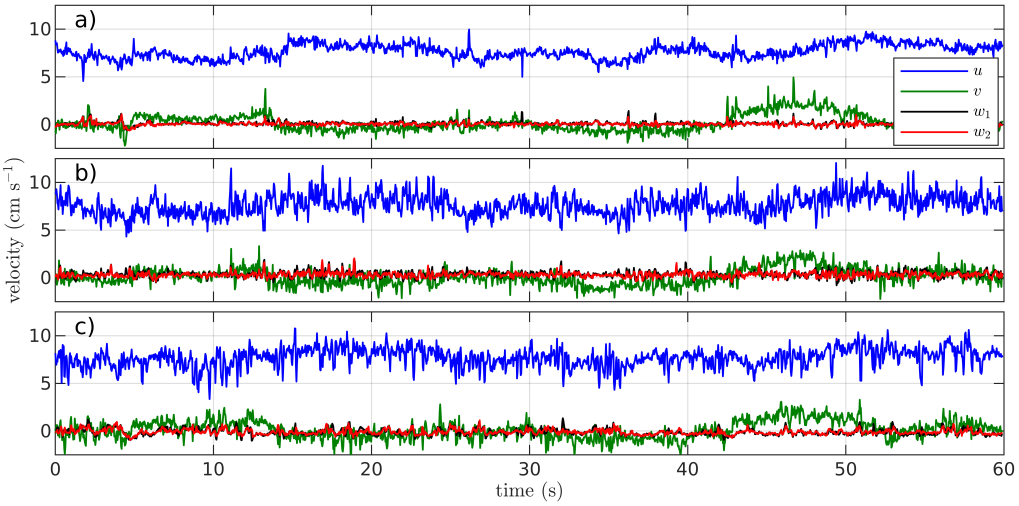

969 FIG. 4. Time series of the four velocity signals recorded by the profiler within the subsurface flow generated
970 by recirculating pumps in the water tank, at three heights above the transducer: a) $h_t = 5.2$ mm; b) $h_t = 4.1$ mm;
971 c) $h_t = 6.4$ mm.

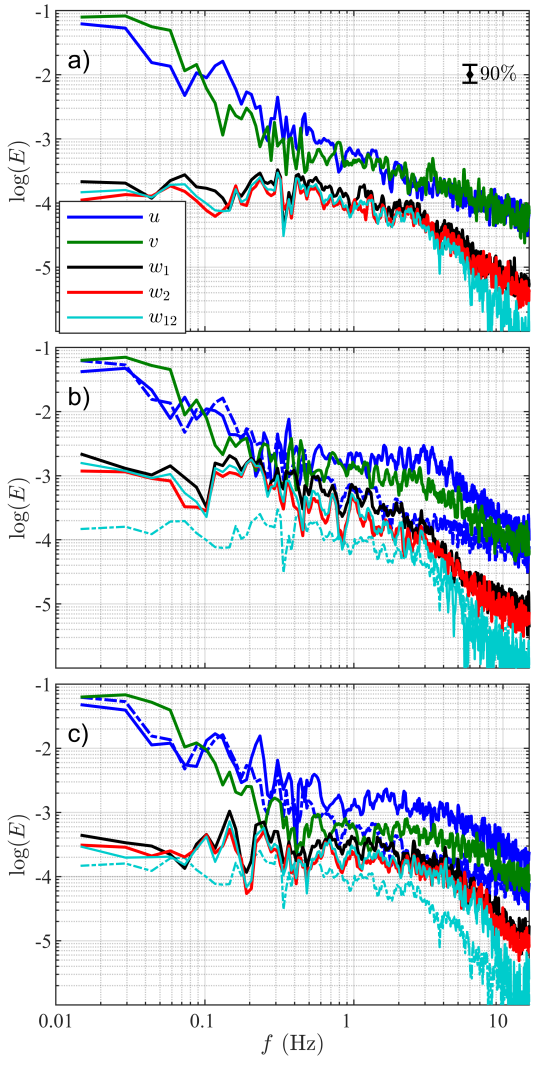

FIG. 5. Frequency spectra and cospectra of the four velocity signals recorded by the profiler within the subsurface water flow generated by recirculating pumps, at three heights above the transducer: a) $h_t = 5.2$ mm; b) $h_t = 4.1$ mm; c) $h_t = 6.4$ mm. The 90 % confidence interval of spectra is given at the top left-hand side of the panel a).

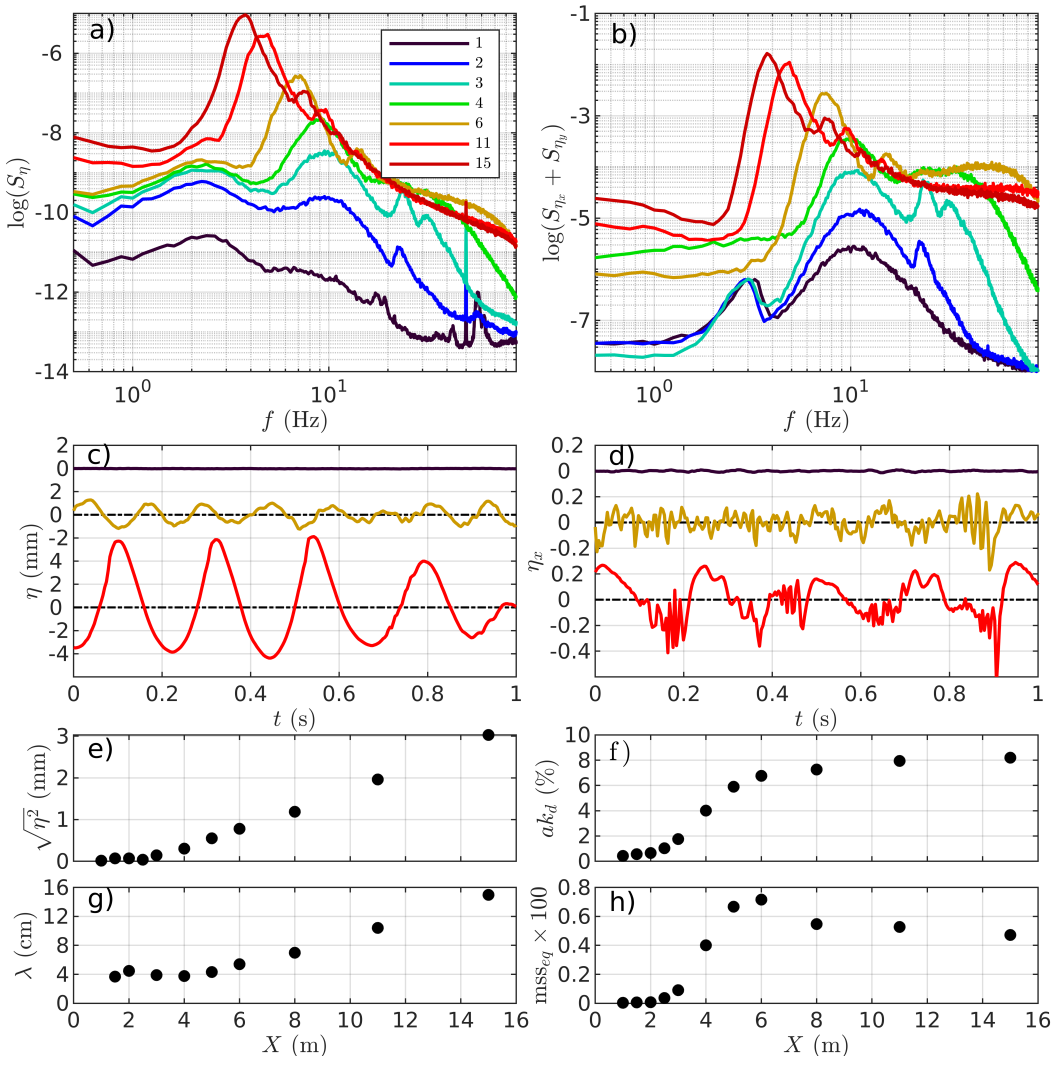

FIG. 6. Wave height (left) and total wave slope (right) characteristics as estimated from single-point probe signals at 4.5 m s^{-1} wind speed: a), b): Frequency spectra at various fetches as displayed in the legend box in meters; c), d) Typical time sequences recorded at 2, 6, and 11 m fetches; e)-h) Variation with fetch of the RMS wave height (e), the dominant wavelength (g), the RMS dominant wave steepness (f), and the total mean square slope of short waves estimated by integration over the equilibrium spectral range (h).

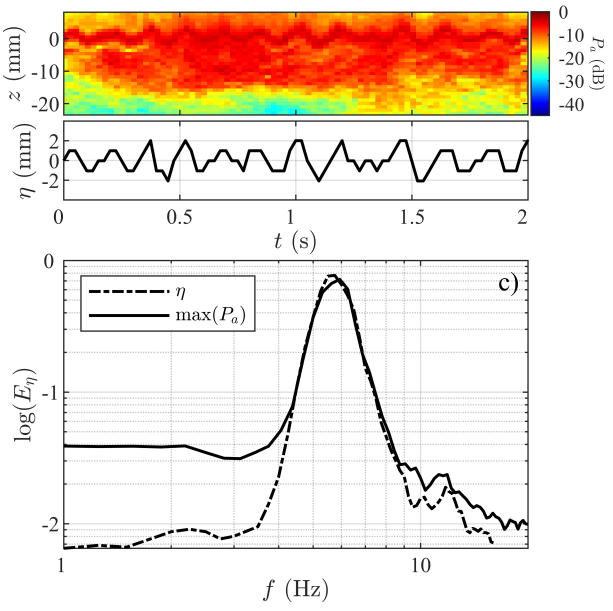

981 FIG. 7. Time variation of (a) the beam-averaged backscattered acoustic power vertical profile observed for
982 8 m fetch and 4.5 m s^{-1} wind speed and (b) the corresponding water surface displacement estimated from the
983 height of acoustic power maxima. c): Frequency spectra of the water surface elevation as measured by the
984 capacitance wave gauge (solid line) and estimated from the height of the acoustic power maxima (dash-dotted
985 line) for the whole time series recorded in this wind and fetch condition.

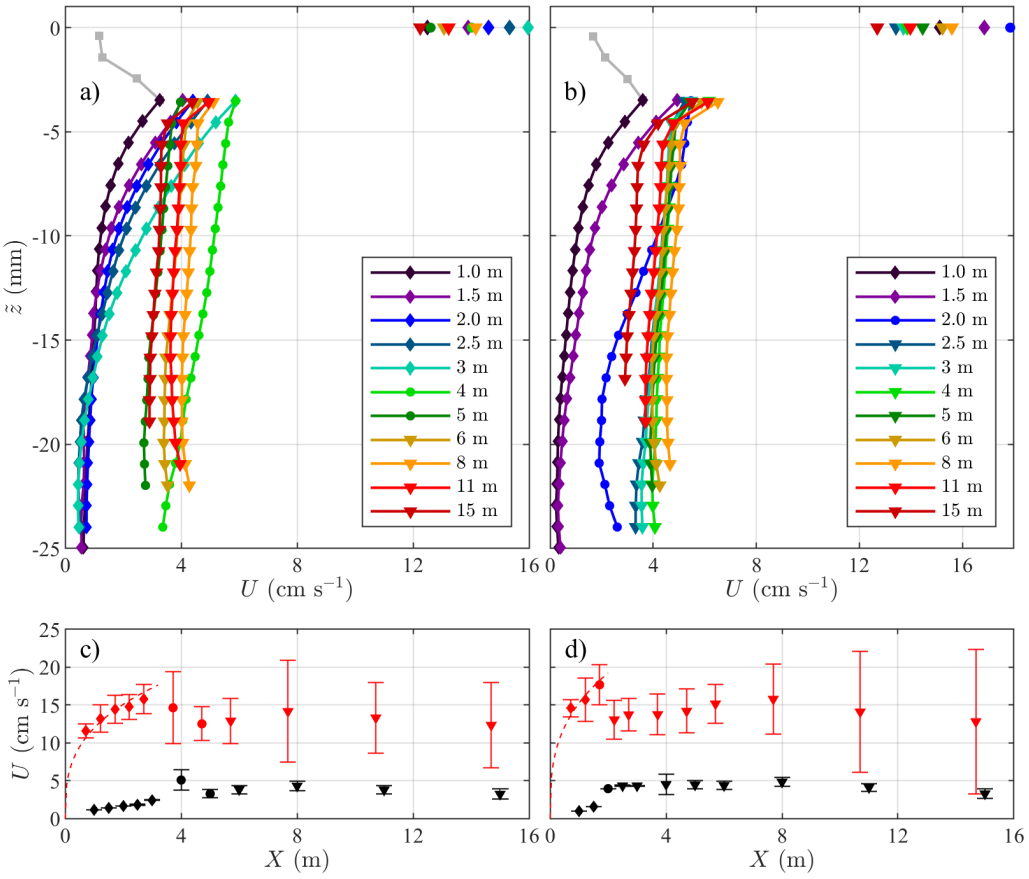

FIG. 8. Mean velocity profiles estimated in a curvilinear coordinate system displayed for all fetches and both wind speeds: a) 4.5 m s^{-1}; b) 5.5 m s^{-1}. The square, round and triangular dots refer to measurements made respectively in the laminar, transitional and turbulent subsurface boundary layer. c), d): Variation with fetch of the mean flow velocity measured by means of surface drifters (red dots) and the profiler at a depth $\tilde{z} = -10$ mm (black dots) for both wind speeds. The error bars represent $\pm$ one standard deviation of the measured values.

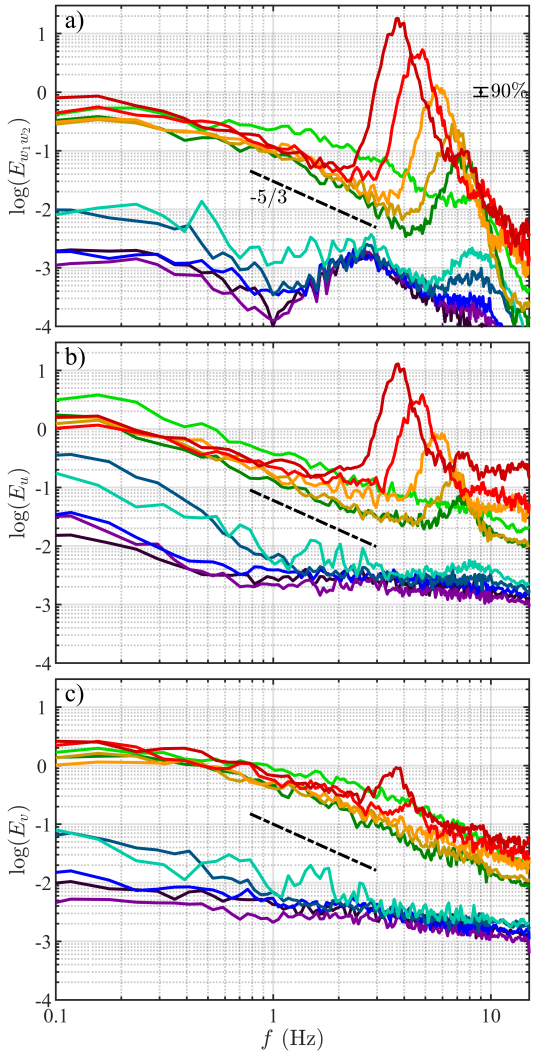

991 FIG. 9. Vertical (a), longitudinal (b) and spanwise (c) velocity spectra observed at depth $\tilde{z} = -10$ mm for
992 all fetches and 4.5 m s^{-1} wind speed. Line colors refer to fetches as indicated in Fig. 8 legend box. The 90 %
993 confidence interval of spectra is given at the top left-hand side of the panel a).

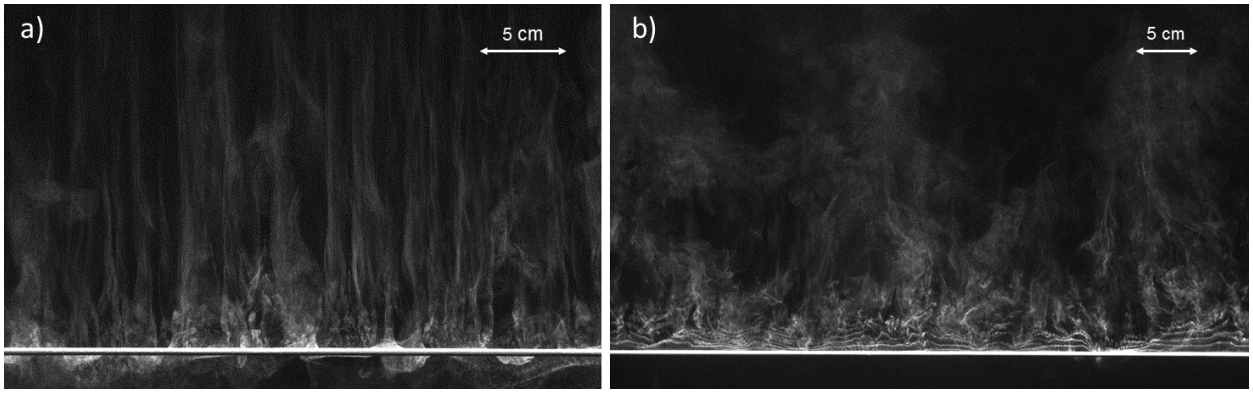

FIG. 10. Views from above of three-dimensional water subsurface flow structures made visible by electrolysis bubbles. a): Laminar streaks observed just before the breakdown to turbulence of the wind-driven water boundary layer at 2 m fetch and 5 m/s wind speed. b): Langmuir circulations observed at 13 m fetch and 4.0 m/s wind speed. The depth of the upper copper electrolysis wire (visualized by the thick horizontal white line) is 3 and 2 cm respectively. Wind blows from the bottom to the top of the images.

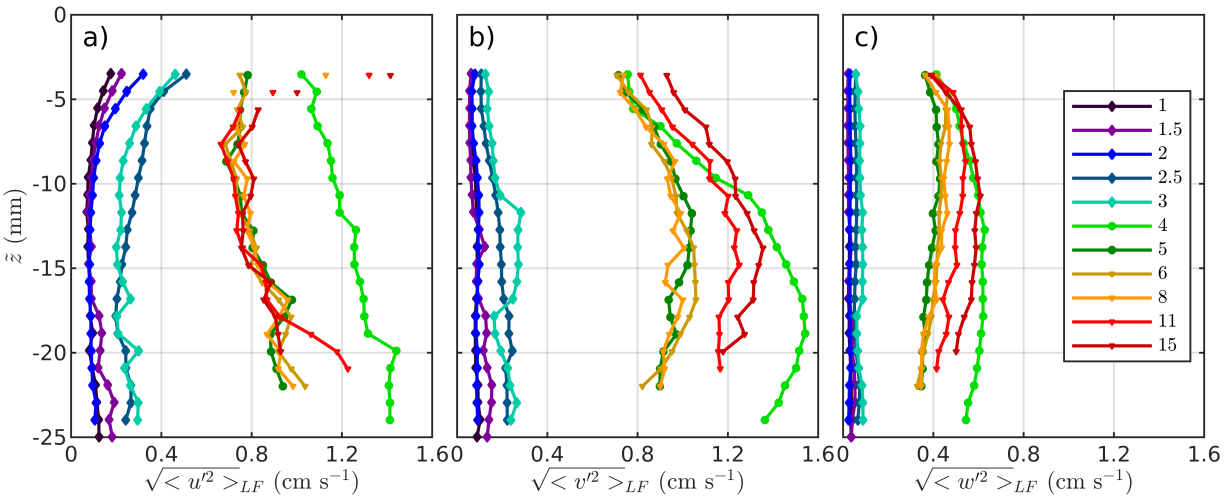

999 FIG. 11. Variation with dominant wave streamline depth $\tilde{z}$ of turbulence intensities estimated from integration
1000 of velocity spectra at low frequencies (i.e. below 1 Hz) displayed for all fetches (given in the legend box in
1001 meters) and 4.5 m s^{-1} wind speed: a): u', b): v', c): w'.

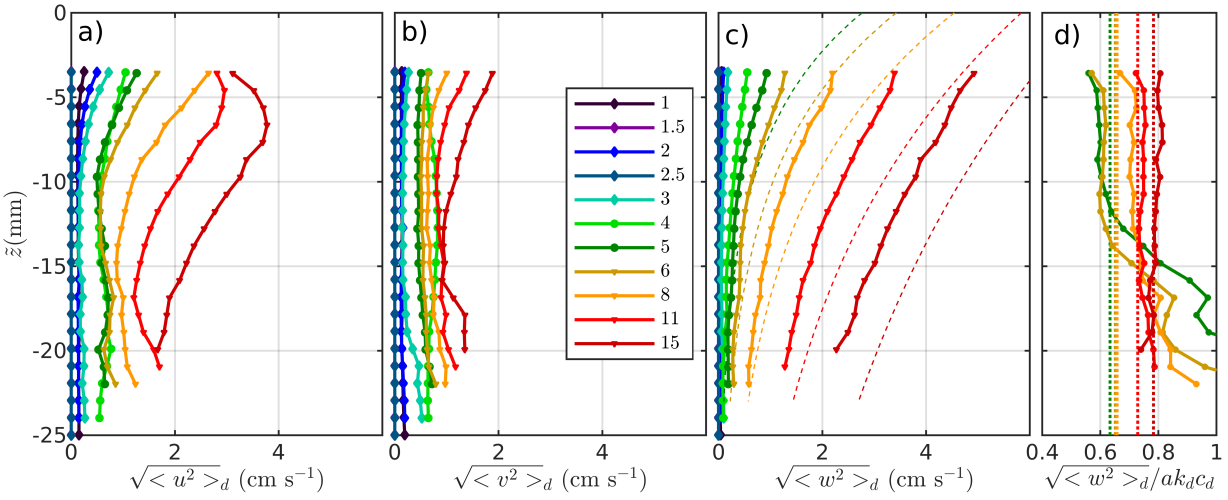

FIG. 12. (a)-(c): Variation with dominant wave streamline depth $\tilde{z}$ of the RMS values of the three velocity components of dominant wave orbital motions as estimated from integration of velocity spectra over the dominant peak, displayed for all fetches and 4.5 m s^{-1}: a): u, b): v, c): w_2. d): Ratio between the measured RMS vertical orbital velocity value and this estimated from measured surface motions by using the linear wave theory as plotted in (c) by dashed lines. Color lines refer to fetches as given in meters in the legend box and the dotted lines, to the respective ratios $ak_d(c_d - U_s)/ak_dc_d$.

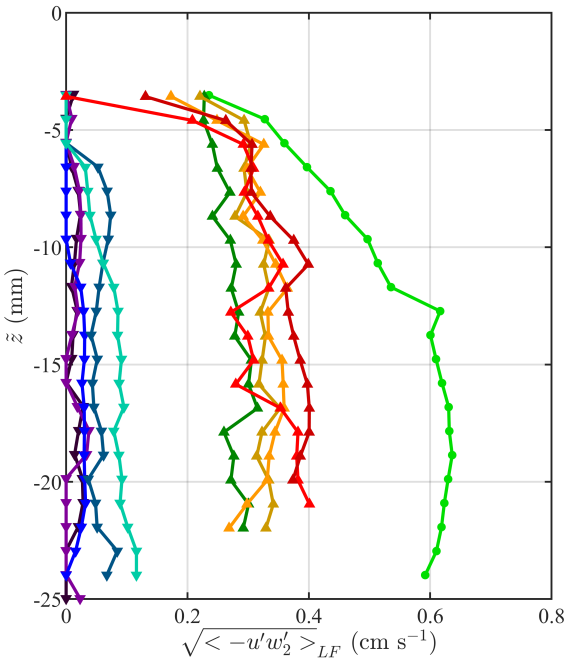

FIG. 13. Variation with dominant wave streamline depth $\tilde{z}$ of the square root of the vertical momentum flux $\sqrt{< u'w'_2 >}$ estimated from integration of velocity cospectra at low frequencies (below 1 Hz), for all fetches and 4.5 m s^{-1} wind speed. Line colors refer to fetches as given in meters in Fig. 11 legend box.